Organic & Biomolecular Chemistry

Accepted Manuscript

ROYAL SOCIETY OF CHEMISTRY

www.rsc.org/obc

Journal Name

ARTICLE TYPE

Cite this: DOI: 10.1039/xxxxxxxxxx

A Few Key Residues Determine the High Redox Potential Shift in Azurin Mutants

Laura Zanetti-Polzi,*[a] Carlo A. Bortolotti,[b] Isabella Daidone[c], Massimiliano Aschi[c], Andrea Amadei[d] and Stefano Corni[a]

Received Date
Accepted Date

DOI: 10.1039/xxxxxxxxxx

www.rsc.org/journalname

The wide range of variability of the reduction potential (E^0) of blue-copper proteins has been the subject of a large number of studies in the past several years. In particular, a series of azurin mutants have been recently rationally designed tuning E^0 over a very broad range (700 mV) without significantly altering the redox-active site [Marshall *et al., Nature*, 2009, **462**, 113]. This clearly suggests that interactions outside the primary coordination sphere are relevant to determine E^0 in cupredoxins. However, the molecular determinants of the redox potential variability are still undisclosed. Here, by means of atomistic molecular dynamics simulations and hybrid quantum/classical calculations, the mechanisms that determine the E^0 shift of two azurin mutants with high potential shifts are unravelled. The reduction potentials of native azurin and of the mutants are calculated obtaining results in good agreement with the experiments. The analysis of the simulations reveals that only a small number of residues (including non-mutated ones) is relevant in determining the experimentally observed E^0 variation *via* site-specific, but diverse, mechanisms. These findings open the way to the rational design of new azurin mutants with different E^0.

1 Introduction

Cupredoxins are a deeply studied group of redox-active proteins in bio-inorganic chemistry. They function as mediators of electron transfer (ET) between proteins in several biologically relevant processes, predominantly in energy conversion cycles but also in diverse biochemical transformations.[1] This family of ET proteins has similar copper primary coordination spheres, with a copper ion coordinated by a cysteine (Cys) and two histidine (His) residues in a trigonal planar geometry plus a weak axial ligand.[2]. In some cupredoxins an additional weak axial interaction between the copper and a backbone carbonyl oxygen is also present. Despite the similarity in the structure of the active site, cupredoxins span a large range of reduction potentials (E^0), from stellacyanin with the lowest potential of about 184 mV vs SHE,[3] to rusticyanin (E^0 = 680 mV vs SHE[4]). This suggests that interactions outside the primary coordination sphere are relevant to determine E^0 in cupredoxins.

In order to unveil the molecular determinants of the high variability of E^0 displayed by cupredoxins, several site-directed mutations involving residues lying in the first and second coordination sphere of such proteins were produced and characterised in the past years extending considerably the range of E^0.[2,5–7] However, there is still a significant lack of knowledge about the mechanism through which non-covalent interactions can tune E^0,[8,9] even though hypotheses have been made on the role of amino acid charges, solvent exposure and hydrogen bonds.[10–18]

Among cupredoxins, Azurin (Az) has served as a paradigmatic test system for a number of experimental and theoretical investigations on biological ET[19–33]. In recent studies[2,6] the reduction potential of Azurin was tuned over a 700 mV range by site-specific mutations designed not to perturb the metal binding site be-

[a]*Center S3, CNR-Institute of Nanoscience , Via Campi 213/A, 41125, Modena, Italy.*
*E-mail:laura.zanettipolzi@nano.cnr.it
[b]*Department of Life Sciences, University of Modena and Reggio Emilia, Via Campi 183, 41125, Modena, Italy.*
[c]*Department of Physical and Chemical Sciences, University of L'Aquila, via Vetoio (Coppito 1), 67010, L'Aquila, Italy*
[d]*Department of Chemical and Technological Sciences, University of Rome "Tor Vergata", Via della Ricerca Scientifica, 00185, Rome, Italy.*

† Electronic Supplementary Information (ESI) available: Additional details on the quantum centre and additional analyses on the mutants' properties. See DOI: 10.1039/b000000x/

yond what is typical for the cupredoxin family of proteins. Those works suggested a decisive role in affecting E^0 of hydrophobic and hydrogen bonding interactions in the secondary coordination sphere, yet the detailed nature and the effects of these interactions are still undisclosed.[9]

In the present study, a theoretical-computational approach similar to quantum mechanics/molecular mechanics (QM/MM) procedures, based on the joint use of molecular dynamics (MD) simulations and a hybrid mixed quantum/classical methodology, the Perturbed Matrix Method (PMM),[34–38] is applied to calculate E^0 in wild-type Az and two of its mutants (N47S/M121L and N47S/F114N/M121L). Both such mutants were experimentally shown to display significant positive shifts of E^0 with respect to the native protein[2,6] though the active site is only moderately perturbed *via* the M121L mutation. In the first mutant (N47S/M121L) a Ser residue characteristic of rusticyanin (the cupredoxin with the highest redox potential) replaces a Asn residue highly conserved in other cupredoxins. An additional mutation (N47S/F114N/M121L) leads to the highest potential reported for Az mutants[2]. These mutants, involving residues located in strategic positions outside the active site, are thus good candidates for the investigation of the role of interactions outside the primary coordination sphere in determine variations of the reduction potential which is a standing, poorly understood issue.

The combined MD-PMM approach has been already applied to calculate E^0 in redox-active proteins[39–41] obtaining results in good agreement with electrochemical measurements. Here, such a computational strategy is used to shed light onto the microscopic mechanism at the basis of the E^0 shift induced by each mutation and to gain insights into the single-residue mechanical-dynamical behaviours underlying the measured variations of such a macroscopic quantity. Besides, the presented analysis suggests novel additional site-specific mutations that could further enlarge the range of variability of E^0 in azurins.

2 Theory and Methods

2.1 Theoretical Background

In MD-PMM calculations,[34–38] similarly to QM/MM procedures,[42–44] a portion of the system to be treated at electronic level is pre-defined (the quantum centre, QC), with the rest of the system described at a classical atomistic level exerting an electrostatic effect on the QC, similarly to QM/MM simulations with electrostatic embedding. With a relatively low computational cost, the MD-PMM can be applied to a very large set of molecular configurations, hence providing the dynamical coupling of electronic properties with classical degrees of freedom. Indeed, the phase space sampling is provided by classical molecular dynamics (MD) and thus a statistically relevant sampling of the QC/environment configurations can be achieved, which is necessary for a proper description of functional properties in dynamical, complex systems. For each configuration of the whole system generated from the MD simulation, the effect of the external environment on the QC eigenstates is included by building and diagonalizing the perturbed electronic Hamiltonian matrix ($\widetilde{H}$) constructed in the basis set of the unperturbed Hamiltonian eigenstates of the QC. Indicating with $\mathcal{V}$ and $\boldsymbol{E}$ the perturbing electric potential and field, respectively, exerted by the environment on the QC:

$$\widetilde{H} \simeq \widetilde{H}^0 + \widetilde{I} q_T \mathcal{V} + \widetilde{Z}_1 \tag{1}$$

$$[\widetilde{Z}_1]_{j,j'} = -\boldsymbol{E} \cdot \langle \phi_j^0 | \hat{\boldsymbol{\mu}} | \phi_{j'}^0 \rangle \tag{2}$$

where q_T, $\hat{\boldsymbol{\mu}}$ and ϕ_j^0 are the QC total charge, dipole operator and unperturbed electronic eigenfunctions, respectively, $\widetilde{I}$ is the identity matrix and the angled brackets indicate integration over the electronic coordinates. The diagonalization of $\widetilde{H}$ provides a set of eigenvectors and eigenvalues representing the QC perturbed electronic eigenstates and energies. More details on this method can be found in the original articles.[34–38] The MD-PMM has been able to provide a reliable modelling of different chemical processes, preserving both the quantum-chemical description of the chemical event and the configurational complexity of the overall molecular environment.[41,45,46]

For the more specific task of calculating E^0 in redox-active proteins, the perturbed electronic ground-state energies are calculated for the QC reduced and oxidised chemical states, providing the perturbed electronic ground-state energy shift. Also, the perturbing environment configurations are obtained by classical MD simulations performed in both the reduced and oxidised ensemble (*i.e.*, with the QC in the reduced and oxidised chemical state, respectively).

The (Helmholtz) free energy change ΔA_I^0 associated to the electron transfer reaction (related to E^0 via E^0=-ΔA^0/F, with F the Faraday constant) for the redox system in the presence of a given number I of ions in solution can be calculated using the following equation:[47]

$$\begin{aligned} \Delta A_I^0 &= -k_B T \ln \left\langle e^{-\beta \Delta \mathcal{U}_{ox\to red}} \right\rangle_{ox} = k_B T \ln \left\langle e^{-\beta \Delta \mathcal{U}_{red\to ox}} \right\rangle_{red} \\ &\approx -k_B T \ln \left\langle e^{-\beta \Delta \varepsilon_{ox\to red}} \right\rangle_{ox} = k_B T \ln \left\langle e^{-\beta \Delta \varepsilon_{red\to ox}} \right\rangle_{red} \end{aligned} \tag{3}$$

In the above equation $\Delta \mathcal{U}_{ox\to red(red\to ox)}$ is the whole system energy change upon reduction (oxidation), $\Delta\varepsilon_{ox\to red(red\to ox)} = \varepsilon_{red} - \varepsilon_{ox}(\varepsilon_{ox} - \varepsilon_{red})$, with ε_{red} and ε_{ox} representing the perturbed ground-state electronic energy of the *red* (reduced) and *ox* (oxidised) chemical states, respectively, and the approximation $\Delta \mathcal{U}_{ox\to red(red\to ox)} \approx \Delta\varepsilon_{ox\to red(red\to ox)}$ is used, *i.e.*, the environment internal energy change associated to the QC reduction is disregarded being exactly zero within the present description.[38] ε_{red} and ε_{ox} are the perturbed electronic ground-state energies evaluated at each MD frame via the MD-PMM approach and averaging

is performed in either the oxidised or reduced ensemble as indicated by the subscript of the angle brackets.

Although Eq. 3 is based on an exact relation in principle, given the sampling problems of finite-time simulations, the best estimate of the reduction free energy is obtained by averaging the values provided by the reduced and oxidised ensembles:[48]

$$\Delta A_I^0 = \frac{-k_B T \ln\left\langle e^{-\beta\Delta\varepsilon_{ox\to red}}\right\rangle_{ox} + k_B T \ln\left\langle e^{-\beta\Delta\varepsilon_{red\to ox}}\right\rangle_{red}}{2} \quad (4)$$

In addition, it must be noted that the estimate of E^0 can be improved by averaging ΔA_I^0 (as provided by Eq. 4) in two ionic atmospheres: one that neutralises the oxidised state of the active site and one that neutralises the reduced state of the active site. In fact, the overall reduction reaction can be written as:

$$\underbrace{(P_{ox}+I^{ox})+e^-+M^+}_{stateA} \to \underbrace{(P_{red}+I^{red})}_{stateB} \quad (5)$$

where $P_{ox/red}$ represents the protein in its oxidised and reduced state respectively, e^- is the transferred electron and M^+ is a positive ion at infinite distance. $I^{ox/red} = N_{M^+}^{ox/red} M^+ + N_{A^-}^{ox/red} A^-$ with $N_{M^+/A^-}^{ox/red}$ the proper numbers of positive (M^+) and negative (A^-) ions to neutralise, respectively, the oxidised and reduced state of the protein. Note that in the present case $N_{M^+}^{ox} = N_{A^-}^{ox} = 0$ and $N_{M^+}^{red} = 1$, $N_{A^-}^{red} = 0$. The path from state A to state B can be also written as:

$$\begin{array}{cc} I & II \\ (P_{ox}+I^{ox})+e^-+M^+ \to & (P_{ox}+I^{red})+e^- \to (P_{red}+I^{red}) \end{array} \quad (6)$$

Analogously, the path from state B to state A can be written as:

$$\begin{array}{cc} III & IV \\ (P_{red}+I^{red}) \to & (P_{red}+I^{ox})+M^+ \to e^-+M^++(P_{ox}+I^{ox}) \end{array} \quad (7)$$

The free energy associated to step I in Eq. 6 is the work necessary to bring the M^+ ion in the vicinity of the oxidised protein from an infinite distance, the free energy associated to step II is the reduction free energy in the ensemble with the proper number of ions to neutralise the reduced state of the protein ($\Delta A_{I^{red}}^0$, as provided by Eq. 4). Analogously, in Eq. 7 the free energy associated to step III is the free energy necessary to remove the ion from the vicinity of the reduced protein to an infinite distance and the free energy associated to step IV is the oxidation free energy in the ensemble with the proper number of ions to neutralise the oxidised state ($-\Delta A_{I^{ox}}^0$). Assuming that the free energy of step I associated to positively charging the oxidised protein hydration shell (*i.e.*, the complex defined by the protein, non-bulk solvent and possibly the counterions) be approximately equal to the free energy of step III associated to negatively charging the reduced protein hydration shell, the free energy change ΔA^0 associated to the overall reaction of Eq. 5 can be written:

$$\Delta A^0 \cong \frac{\Delta A_{I^{red}}^0 + \Delta A_{I^{ox}}^0}{2} \quad (8)$$

Note that the approximate equality of the free energies of steps I and III is based on the assumption that for both the oxidised and reduced protein in the typical experimental conditions (temperature, pressure, ionic strength etc.) the corresponding equilibrium ionic cloud is defined by the counterions neutralising the overall protein charge and hence positively(negatively) charging the oxidised(reduced) protein hydration shell corresponds to a free energy increment.

2.2 Simulated Systems

MD simulations and subsequent MD-PMM calculations of wild-type Az (WT Az) and two mutants (N47S/M121L, hereafter called Mut1 and N47S/F114N/M121L, hereafter called Mut2) are here performed. In Figure 1, a schematic representation of the copper binding site and surrounding secondary coordination sphere of wild-type Az (panel A), Mut1 (panel B) and Mut2 (panel C) is reported. The copper site in WT Az contains three strong ligands: His46, Cys112 and His117, that form a trigonal planar geometry around the metal centre, and two weak axial ligands: Met121 and Gly45.[2] The mutants here analysed have all three of the strong ligands conserved, while the weak axial ligand Met121 is replaced by a Leu and Asn47 is changed to Ser. These two mutations are present in both Mut1 and Mut2. In addition, Phe114 is changed to Asn in Mut2. As this last mutation does not involve the active site, Mut1 and Mut2 share the same active site.

2.3 Molecular dynamics simulations

For WT Az and Mut1 the crystallographic structures (Pdb code 4AZU and 3JT2, respectively) are used as starting structures for the MD simulations. As the crystallographic structure for Mut2 is not available, the initial structure for this mutant is obtained by replacing Phe114 with Asn in the structure of Mut1.

The AMBER99 force field parameters[49] are adopted for the protein with all Lys, His35 and His83 in the protonated form. To properly model the active site, the following modifications to the standard force field are introduced. Bonds are added between the copper and its five ligands at the crystallographic bond length for both WT Az and the two mutants. As the crystallographic structure for Mut2 is not available as mentioned above, the same structure of the active site (*i.e.*, the same values for bond lengths and bond angles, see below) is assumed for the two mutants. More details on the binding of Leu121 in Mut1 and Mut2 are given in the Electronic Supplementary Information (ESI). All the

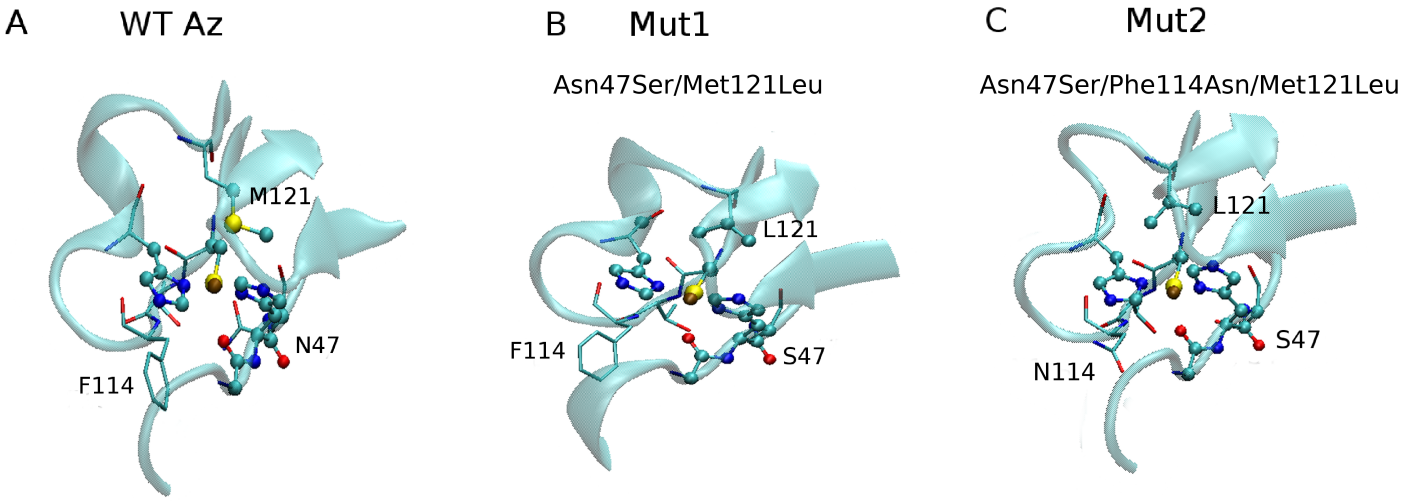

Fig. 1 Schematic representation of the copper binding site (in licorice) and surrounding secondary coordination sphere of wild-type Az (panel A), Mut1 (panel B) and Mut2 (panel C). The atoms that also belong to the quantum centre are highlighted in ball-and-sticks.

angles coming from these bonds are set at the crystallographic value with bending force constants taken from the literature.[50] Lennard-Jones parameters for the copper are also taken from the literature.[50] Nonbonded interactions between the copper and its five coordinating atoms are treated as in van den Bosch *et al.*.[25] The same parameters are used for the oxidised and reduced state of the QC. More details on the parameters used are provided in the ESI.

MD simulations are performed for both the reduced and the oxidised form of WT Az and the two mutants. The two oxidation states are obtained by changing the atomic charges of the protein active site (see next subsection). In addition, each redox state is simulated for all the species (WT and the mutants) in two ionic atmospheres (see Theory section): the one that neutralises the oxidised state (no ions) and the one that neutralises the reduced state (1 Na^+ ion). A Na^+ is chosen as counterion in the protein ionic cloud as it does not imply a change in the protonation state of a specific residue (as it would have been if e.g. a H^+ ion was added). The Na^+ is on the contrary free to move inside the simulation box, thus mimicking the experimental conditions (at neutral pH) typically involving the presence of diluted electrolytes.

Each structure is solvated in a periodic rhombic dodecahedral box filled with TIP3P water molecules.[51] After a solute optimisation and a subsequent solvent relaxation, each variant is gradually heated from 50 K to 300 K using 100 ps MD simulations. The trajectories are then propagated for 100 ns in the NVT ensemble with isokinetic temperature coupling[52] keeping the temperature constant at 300 K. For each species, 400 ns of MD simulation were thus performed. Periodic boundary conditions and a non-bond pairlist cutoff of 9.0 Å are used and the long-range electrostatic interactions are treated with the particle mesh Ewald method.[53] The bond lengths are fixed[54] and a time step of 2 fs for numerical integration of the equations of motion is used. The simulations are performed with the GROMACS software package.[55]

Configurations of the whole system generated from the MD simulation and collected every ps are used to calculate the perturbed electronic ground-state energies via the MD-PMM approach (see section 2.1).

2.4 Quantum chemical calculations

The atomic charges for the copper and its ligands in the reduced and oxidised chemical states are obtained from density-functional theory (DFT) quantum-chemical calculations by using the Amsterdam Density Functional (ADF) software[56] as previously done for the same system.[25] Multipole-derived charge analysis is used to obtain the atomic charges.[57]

A QC to be explicitly treated at the electronic level is necessary for the MD-PMM procedure to be applied (see Theory Section). The atoms belonging to the QCs of WT Az and the two mutants are highlighted in ball-and-sticks in Figure 1 (see also Figure S1 in the ESI). Here, the QC is the copper binding site plus the alpha carbon and the backbone nitrogen of residue 47 (properly saturated with hydrogen atoms). The choice of the QC and the hydrogen bonding pattern of the sulphur of Cys112 are discussed in the ESI. The crystallographic structure of the two QCs is refined by performing quantum-chemical geometry optimisation (in both the reduced and oxidised state of the QC) with the ONIOM computational technique.[58] A 2-layer ONIOM optimisation using mechanical embedding is performed: the QC geometry is optimised

with the Becke's three parameters exchange and Lee, Yang and Parr correlation functionals (B3LYP) with a triple-zeta valence basis set while the rest of the system is kept frozen and treated with the UFF force field.[59] The inclusion of dispersion corrections[60] for the geometry optimisation of the QC was tested, showing no relevant variations. More details on the optimised geometries of the two QCs are given in the ESI.

For both QCs, quantum chemical calculations are performed on the optimised geometry of the isolated QC for both redox states (Cu(I) and Cu(II)) at the Time Dependent Density Functional Theory (TD-DFT) level with the M06 functional[61] and a triple-zeta valence basis set (TZV[62]). The CAM-B3LYP functional[63] was also tested. Both functionals provide an energy difference between the reduced and oxidised isolated QC ≈6 kJ/mol higher for Mut1 and Mut2 with respect to WT Az. However, the unperturbed contribution to the calculated E^o provided by CAM-B3LYP slightly worsens (by ≈10 kJ/mol) the agreement with the experimental data with respect to M06. Therefore, the M06 functional was chosen for all the subsequent calculations. All quantum chemical calculations are carried out using the Gaussian03 package.[64]

For each redox state, a thirteen-dimensional Hamiltonian is evaluated and diagonalized at each step of the MD simulations according to the MD-PMM procedure (see Theory section).

3 Results and Discussion

3.1 The Reduction Potentials of native Az, Mut1 and Mut2: comparison with experimental data

As mentioned in the Methods section, MD simulations are performed in two ionic atmospheres: one that neutralises the oxidised state of the active site and one that neutralises the reduced state of the active site. In both these ionic atmospheres simulations are performed with the active site in its reduced and oxidised state. The final results of the calculated potentials (reported in Table 1 together with the corresponding experimental measurements) are calculated as the mean value of E^0 calculated for each of the four MD simulations (for each variant). For all the investigated species, the comparison between the calculated and experimental absolute values of the redox potentials shows an underestimation of the calculated E^0 of about 250 mV. Such underestimation is systematic over the three species and is likely to be due to the accuracy of DFT calculations. Remarkably, such a disagreement does not affect the shift between the values calculated for the three species. As a matter of fact, the calculated shifts due to the mutations are in agreement with the experimental measurement within the statistical errors (see Table 1).

The perturbed energy difference $\Delta\varepsilon$ used to calculate E^0 for the three species (see Theory section) is reported as a function of time for the MD simulations with the reduced QC (reduced ensemble) and oxidised QC (oxidised ensemble) in Figure 2. Note that in the reduced ensemble $\Delta\varepsilon = \varepsilon_{ox} - \varepsilon_{red}$ and in the oxidised ensemble $\Delta\varepsilon = \varepsilon_{red} - \varepsilon_{ox}$. The energies reported in the Figure are calculated from the MD simulation in the ionic atmosphere that neutralises the oxidised state (the ionic atmosphere that neutralises the reduced state provides a qualitatively identical picture). The shift in the energy trend between the three species that results in the raise of the calculated E^0 can be easily observed in the Figure.

According to Eqs. 1 and 2, $\Delta\varepsilon$ depends on the difference between the unperturbed ground state energies, on the electrostatic potential exerted by the perturbing environment on the QC and on the $\widetilde{Z}_1$ term (*i.e.*, the interaction between the electric field exerted by the perturbing environment and the dipole moments of the QC). Such last term has a lower effect with respect to the second one in determining the absolute value of E^0. To better characterise the origin of the E^0 shift upon mutation, the contribution of the second and third term to the shift are calculated separately showing a contribution of the $\widetilde{Z}_1$ term to the total shift of ≈ 60 mV in Mut1 and ≈ 30 mV in Mut2. An additional test shows also that these contributions arise from the electrostatic interaction of the environment with the ground state of the QC. In a previous work[18], the removal of the C=O dipole near the sulphur of Cys112 due to the N47S mutation was found to decrease the electron density on the sulphur ligand. According to the above discussion, the present calculations do not evidence a relevant rearrangement of the electronic structure of the QC due to the presence (or removal) of the Asn47 C=O dipole, since the interaction with the classically-described environment, which includes the Asn47 C=O group, does not significantly mix the unperturbed ground and excited states. Variations of the hydrogen bonding (HB) pattern of Cys112 upon mutation could determine as well a rearrangement of the electronic structure of the QC. The sulphur of Cys 112 is indeed at HB distance from the backbone NH of both residue 47 and residue 114. However, the crystallographic structure of Mut1 does not evidence any relevant change in the HB between Cys112 and residue 47 upon the N47S mutation. Accordingly, the population analysis of charge and spin density from the quantum calculations does not reveal any difference between the two QCs (that include the backbone NH of residue 47). Regarding the HB of Cys112 with the backbone NH of residue 114 (that is included in the classically-described environment), the analysis of the MD simulations did not evidence upon the F114N mutation any relevant change in such a HB pattern.

3.2 Molecular Determinants to the Redox Potential Shifts

First, the effect of the mutation M121L that is inside the active site will be considered. According to Eq. 1 $\Delta\varepsilon$ contains, among other contributions, the difference between the unperturbed ground state energies of the QC. Such a difference is obviously a constant along the energy trajectory. However, since the QC of Mut1 and Mut2 is different from the one of WT Az, the unperturbed

Table 1 Absolute reduction potentials of WT Az, Mut1 (N47S/M121L) and Mut2 (N47S/F114N/M121L). E^0 is the average of the values calculated in the two ionic atmospheres and in the two redox states (see Eq. 8). The experimental values are taken from Farver *et al.*.[6] To compare absolute redox potentials, the IUPAC recommended 4.420 V value for the hydrogen semi- reaction[65,66] was added to the experimental E^0 versus SHE

	Wild Type Az	Mut1	Mut2
Calculated E^0 (V)	4.439±0.024	4.684±0.017	4.810±0.020
Experimental E^0 (V)	4.706±0.008	4.929±0.003	5.061±0.009
Calculated $E^0 - E^0_{WTAz}$ (V)		0.245±0.029	0.371±0.031
Experimental E^0-E^0_{WTAz} (V)		0.223±0.008	0.355±0.012

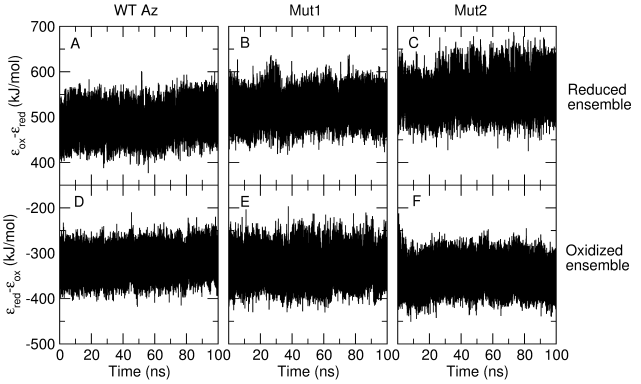

Fig. 2 Time course of the difference between the perturbed ground-state electronic energy of the reduced and oxidised chemical states calculated from the reduced (panels A to C) and oxidised (panels D to F) simulations of WT Az (panels A and D), Mut1 (panels B and E) and Mut2 (panels C and F) in the ionic ensemble that neutralises the oxidised state.

energy difference of the mutants differs from the one of WT Az. $\Delta\varepsilon^{unp} = \varepsilon^{unp}_{red} - \varepsilon^{unp}_{ox}$ is indeed ≈ 65 mV lower in the two mutants. This shift is due to the replacement in the QC of the weak axial ligand Met121 with Leu and is thus the result of the different chemical interaction between the copper and these two ligands. Interestingly, the extent of this shift almost corresponds to the E^0 shift experimentally reported as a consequence of the M121L mutation only (≈ 83 mV).[2,6] The comparison between the calculated and the experimental result thus suggests that the intrinsic nature of the direct chemical interaction in the copper binding site is a major contribution to the experimental E^0 shift associated to the M121L mutation.

As previously mentioned, the most important contribution to the fluctuations of $\Delta\varepsilon$ around the unperturbed ground state energy difference along the trajectory is given by the electrostatic potential felt by the QC. Such a fluctuation is also determined by the additional contribution of the higher order term $\widetilde{Z}_1$ (see Eq. 1,2). To gain insights into the molecular mechanism that determines the overall E^0 variation upon mutation of the aforementioned residues, the electrostatic potential exerted on the QC by each residue of the protein has been analysed. Such analysis accounts indeed for site-specific contributions to the perturbed ground state energy and the difference of the single residue electrostatic potential upon mutation is thus meaningful to identify the sites that most contribute to the E^0 shift. In addition, the electrostatic potential exerted by water is also calculated. To evaluate also the single-residue contribution of the $\widetilde{Z}_1$ term to the overall fluctuation of $\Delta\varepsilon$, a series of PMM calculations are performed for a selected number of residues taking into account only one residue. From this analysis it emerges that also at the single-residue level the electrostatic potential is the most significant term and that the $\widetilde{Z}_1$ term is a higher order correction. In addition, it emerges that the residues that show a relevant electrostatic potential contribution are also the ones showing the most significant $\widetilde{Z}_1$ terms, confirming that the analysis of the single-residue electrostatic potential is meaningful to identify the sites that most contribute to the E^0 shift.

In Figure 3, the contribution to $\Delta\varepsilon_{ox\rightarrow red}$ due to the electrostatic potential, eV, is plotted for each residue and water both for Mut1 with respect to WT Az (panel A) and for Mut2 with respect to WT Az (panel B). The reported values are obtained by averaging the mean electrostatic potential in all the ensembles. In the Figure the mutated residues are highlighted in red, the contribution of water is highlighted in blue and the residues that show the higher difference with respect to WT Az are highlighted in green. In particular, the green coloured residues are those that show a $\Delta(eV)$ equal or larger than ± 7.5 kJ/mol (78 mV). Such threshold value is chosen as it is twice the higher error on the E^0 shift (see Table 1), ensuring that the variations taken into account are actually relevant. The residues with a positive(negative) $\Delta(eV)$ raise(lower) E^0. In what follows, the two mutants are analysed separately.

3.2.1 Analysis of the N47S/M121L Mutant (Mut1)

The residues that most contribute to the raise of E^0 in Mut1 are His35 and the mutated Ser47 (see Figure 3, panel A). These are thus more in depth analysed in order to clarify the possible dynamic or structural determinants at the basis of their effect.

As previously mentioned, residue 47 is considered important

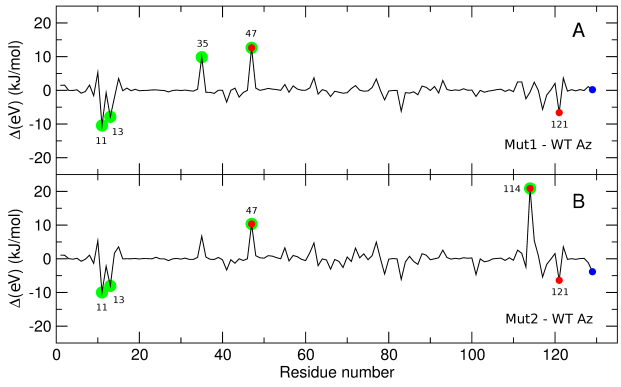

Fig. 3 $\Delta(eV) = eV_{Mut} - eV_{WTAz}$ is plotted for each residue and water for Mut1 (panel A) and Mut2 (panel B). eV is the mean value along the trajectory of the contribution due to the electrostatic potential to the reduction ground state energy difference obtained by averaging the results in the reduced and oxidised ensemble in the two ionic atmospheres. The mutated residues are highlighted in red, the contribution of water is highlighted in blue and the residues that show the higher difference with respect to WT Az are highlighted in green.

in the active site as it is thought to affect the hydrogen bonding pattern of the copper ligands and thus to affect the rigidity of the copper binding site.[2,18] In particular, the analysis of several cupredoxin structures and the comparison with that of rusticyanin (Rc) revealed a Ser residue (Ser86 in Rc) at a position corresponding to a highly conserved Asn in other cupredoxins (Asn47 in WT Az). The N47S mutation in WT Az introduces a hydroxyl group at distances from the sulphur of Cys112 and from the backbone amide nitrogen of Thr113 similar to those found in Rc.[2] These distances are thus analysed along the trajectories of the mutant both in the reduced and in the oxidised ensemble and compared to the distance between the side chain carboxyl group of Asn47 in WT Az and the same atoms. Such analysis interestingly reveals that the N47S mutation affects the interaction between the two loops containing the ligands (loop 1, from residue 42 to residue 47 and loop 2, from residue 110 to residue 122, see Figure 4, panel E[6]). This can be observed from Figure 4, panels A to D, where the distribution of the distances sampled along the trajectory between the side-chain oxygen of residue 47 and both the sulphur of Cys112 (OS distance) and the backbone nitrogen of Thr113 (ON distance) are reported for WT Az (panels A and B) and Mut1 (panels C and D) in the reduced (panels A and C) and in the oxidised (panel B and D) ensemble in the two ionic atmospheres. In the reduced ensemble the sampling of two states is well evident: a state in which the interaction between the two loops is stronger (at small ON/OS distances) and a state in which such interaction is weaker (at large ON/OS distances). The large-distance state is much more sampled by the mutant with respect to WT Az. In the oxidised ensemble the population of these two states is not as evident as in the reduced ensemble but an increase of the two distances upon mutation is anyway noticeable.

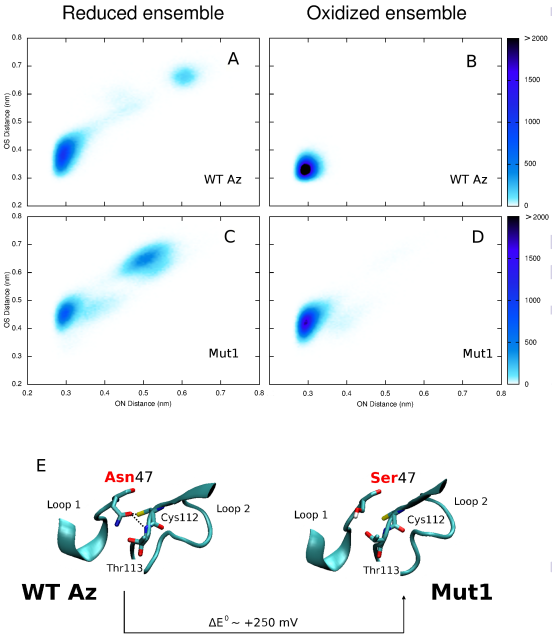

Fig. 4 Panels A to D: Colour maps representing the distribution of distances between loop 1 and loop 2 along the MD simulations. "ON Distance" refers to the distance between the side-chain oxygen of residue 47 and the backbone nitrogen of Thr 113; "OS Distance" refers instead to the distance between the same oxygen and the sulphur of Cys112. Panels A and B report the data for WT Az (A: reduced, B: oxidised), panels C and D for Mut 1 (C: reduced, D: oxidised). The colour code represents the number of points at the corresponding ON/OS distances. Panel E: schematic representation of the weakening of the interaction upon N47S mutation between the two ligand containing loops: loop1 (residues 42-47) and loop 2 (residues 110-122). The increase in E^0 due to this weakening turns out to be around 250 mV, as discussed in the text.

Such results signal a weakening of the interaction between loops 1 and 2. The possible effect on E^0 of this weakening can be brought out by calculating E^0 of the mutant on the two sub-populations: the first at small ON/OS distances and the second at large OS/ON distances. The threshold values for the distances are chosen at the minimum between the peaks of the bimodal distribution of the distances in the reduced ensemble and are 0.4 nm for the $O_{47}N_{113}$ distance and 0.55 nm for the $O_{47}S_{112}$ distance. The calculation is performed in both the reduced and the oxidised ensembles in the ionic atmosphere that neutralises the oxidised state. The resulting values of E^0 (obtained averaging the values calculated in the reduced and oxidised ensemble) show a relevant shift of E^0 due to the weakening of the interaction: higher ON/OS distances correspond to a ≈250 mV higher E^0. Such a result is likely to depend on both the enlargement of the distance

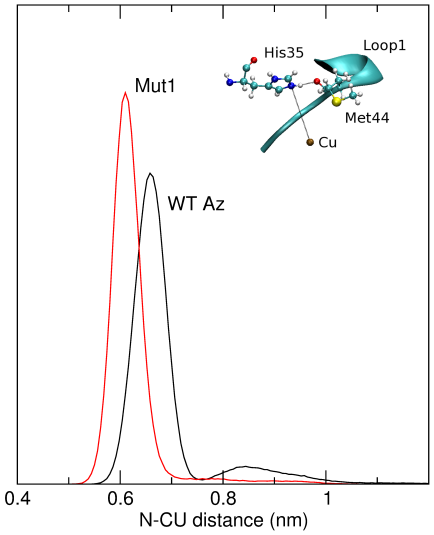

Fig. 5 Distribution of the distance between the ε (unprotonated) nitrogen of His35 and the copper for WT Az (black) and for Mut2 (red) obtained from the average between the reduced and oxidised ensemble simulations in the two ionic atmospheres. In the inset, a schematic representation of such a distance is depicted.

between the negatively charged side-chain oxygen from the active site (destabilising the oxidised state) and on the removal of the C=O dipole upon mutation creating a different electric field on the active site.

The other residue that contributes to the raise of E^0 in Mut1, according to the analysis of the electrostatic potentials (see Figure 3), is His35. The analysis of this residue reveals that its contribution could be triggered by the effect of the N47S mutation on the behaviour of loop 1. The different behaviour of residue 47 in WT Az and Mut1 has an effect on the whole loop and hence on the position of His35, hydrogen-bonded to loop 1 via Met44, that gets closer to the active site upon mutation. As His35 is positively charged, its lower distance from the active site has a destabilising effect on the oxidised state thus contributing to the raise of E^0. It can be observed from Figure 5 that the most probable distance between the ε nitrogen of His35 and the copper is 0.05 nm lower in Mut1 than in WT Az. As the net charge of His is mainly located on the side chain such a variation has an average effect on the electrostatic potential (calculated as 0.05 nm times the charge on Nε) of ≈ 14 kJ/mol (145 mV), very close to the effect obtained calculating the difference between the electrostatic potential exerted by His35 on the QC in WT Az and in Mut1 along the whole trajectories (10 kJ/mol, 104 mV).

3.2.2 Analysis of the N47S/F114N/M121L Mutant (Mut2)

According to the analysis of the electrostatic potentials (see Figure 3), panel B, the contributions of residues 35 and 47 are maintained in Mut2, confirming the experimental hypothesis that the N47S and F114N mutations individually perturb separate areas of the protein leading to an additive effect on E^0.[2] The contribution of residue 35 is less relevant but still present and close to the threshold chosen to identify the significant contributions (6.7 kJ/mol vs 7.5 kJ/mol). The distances between the side-chain oxygen of Ser47 and both the sulphur of Cys112 and the backbone amide nitrogen of Thr113 are analysed also for Mut2 providing the same picture obtained for Mut1 (see ESI).

An additional relevant contribution to the raise of E^0 of the mutated residue Asn114 is clear in Figure 3, panel B. It has to be considered that in this case the mutation changes the intrinsic nature of the residue: a non-polar residue with a hydrophobic benzyl side chain is substituted by a polar residue with an amide functional group with hydrogen bonding capabilities. To roughly estimate the role of the polarity of the side chain of the mutated residue, a test is performed calculating the electrostatic potential exerted by residue 114 along the Mut2 trajectory (both in the reduced and oxidised ensemble) by substituting its real atomic charges (as provided by the force field) with smaller point charges to mimic the charge distribution of Phe. Such a test reveals that the positive $\Delta(eV)$ increases by ≈ 13 kJ/mol (137 mV) upon the F114N mutation as a consequence of the change of the residue polarity. It has to be remarked that this test provides only a qualitative estimation of such an effect. However, it clearly emerges that the change in the residue polarity is the dominant effect in determining the raise of E^0 upon the F114N mutation. Yet, it emerges also that there is a further non negligible contribution to the electrostatic potential that likely arises from the different dynamic behaviour of the mutated residue and in particular from its capability to form HBs. The analysis of the HB pattern of residue 114 with the rest of the protein shows that for both WT Az and Mut2 the backbone oxygen of residue 114 is steadily hydrogen bonded to the backbone nitrogen of His117. Two additional HBs are formed by Asn114 in Mut2: between its side chain nitrogen and the backbone oxygen of Val43 and between its side chain oxygen and the backbone nitrogen of Gly45. These two HBs both involve loop 1 and are thus likely to have an effect on E^0. This effect can be estimated by calculating separately the E^0 values from the subset of structures corresponding to the formed HB and from the one corresponding to the broken HB. Along the trajectory this last situation is indeed also sampled (see Figure 6 where the distribution of the ON distances for the two HBs is reported as the average of the reduced and oxidised ensemble in the two ionic atmospheres). As the formation and rupture of the two HBs occurs in an uncorrelated way along the trajectories, the calculation is performed separately for the two HBs.

For the Asn114-Val43 HB the calculation of E^0 on the two subpopulations provides very similar results: the E^0 value calculated when the HB is formed differs from the one calculated when the HB is broken by 3 kJ/mol, *i.e.* well within the typical error on cal-

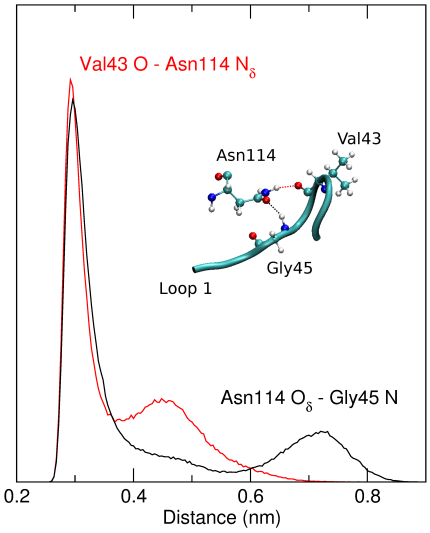

Fig. 6 Distribution of the distance between the side chain nitrogen of Asn114 and the backbone oxygen of Val43 (red) and between the side chain oxygen of Asn114 and the backbone nitrogen of Gly45 (black) in Mut2 obtained from the average between the reduced and oxidised ensemble simulations in the two ionic atmospheres. In the inset, a schematic representation of the two HBs is depicted.

culated redox potentials. The formation of this HB seems thus not to have a direct effect on E^0. On the contrary, the same calculation for the Asn114-Gly45 HB provides a value of $E^0 \approx 9$ kJ/mol (94 mV) higher when the HB is formed with respect to when it is broken. In summary, the hydrogen bonding of the mutated residue with one of the copper ligand perturbs the copper binding site leading to a raise of E^0.

The presence of these HBs is in agreement with the experimental crystallographic findings. The crystal structure shows indeed that the F114N mutation places a HB donor near the backbone of Gly 45.[2] The authors pointed out that, as X-ray crystallography is not always able to distinguish between oxygen and nitrogen atoms in a molecule, the positions of the oxygen and nitrogen on the side chain of Asn 114 could be reversed, *i.e.*, as found in the present MD simulations and in agreement with previous calculations.[18] The resulting position of the amide nitrogen was previously suggested to disrupt the hydrogen-bonding interactions between the copper ligand His 117 and other parts of the protein.[2] However, according to the present MD simulations, the HB pattern of His117 is not affected by the F114N mutation (see ESI) and the raise of E^0 is instead directly ascribable to the mutated residue, as a consequence of both its polar nature and its changed HB pattern.

3.2.3 Hints for Additional Mutations

An interesting feature that emerges from the analysis of the contribution of the electrostatic potential to the perturbed ground state energy is the negative $\Delta(eV)$ at residue 11 and 13 for both Mut1 and Mut2 (see Figure 3). As previously mentioned the residues with a negative $\Delta(eV)$ tend to lower E^0: the mutations performed have thus at these specific sites an effect that is adverse to the overall E^0 positive shift upon mutation. An additional mutation at residues 11 or 13 may thus further enlarge the range of variability of azurins' redox potential reaching an even higher E^0. Residue 11 is a negatively charged residue (Asp) located in a loop that connects two β-strands, *i.e.* in a stable part of the protein. It is also near the active site and in particular near the two histidines that bind the copper and the mutated axial ligand (Met121 in WT Az and Leu121 in Mut1 and Mut2, see Figure 7). The vicinity to the axial ligand could be the key to understand its tendency to lower E^0 upon the M121L mutation. The interaction between the copper and Leu121 is indeed weaker than the one between the copper and Met121 and leads thus to a less tight active site that is more sensitive to the effect of the charged groups facing that side of the active site. As Asp11 is negatively charged a less screened interaction of this residue with the active site tends to stabilise the oxidised state and thus to lower E^0. The mutation of Asp11 with a residue having a side chain with comparable steric hindrance but a zero charge (as for example Asn) could thus lead to a higher E^0. A similar effect could also be at the origin of the contribution of Met13 in lowering E^0: the active site might more efficiently interact with the negatively charged sulphur or the backbone oxygen of Met13 in the mutants thus leading to a stabilisation of the oxidised state. However, as Met13 does not carry a net charge it is more difficult to predict the effect on E^0 due to a mutations at that site. The effect of such a mutation could indeed strongly depend on the choice of the mutated residue and on the way it interacts with other residues in its neighbourhood. In any case, the present data suggest that mutations performed in the small loop from residue 11 to residue 13 are likely to have relevant effects on the reduction potential.

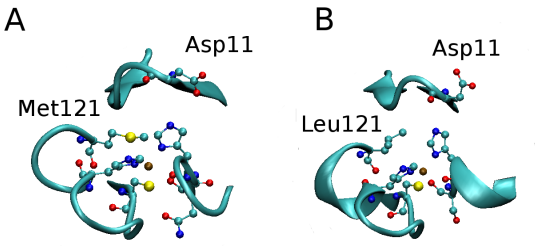

Fig. 7 Two representative snapshots that highlight the position of Asp11 with respect to the active site (in ball-and-sticks) in WT Az (panel A) and in the M121L mutants (panel B). The loops that contain the copper ligands (loop 1 and 2) and the loop that contains residue 11 together with the two strands connected by such a loop are also depicted.

4 Conclusions

In the present work state-of-the-art MD simulations and hybrid quantum/classical calculations allowed to unravel the microscopic mechanisms that determine the experimentally measured variations of E^0 upon mutation in azurin.

Azurin and two of its variants have been studied here: N47S/M121L and N47S/F114N/M121L. Using a hybrid quantum mechanics/molecular mechanics methodology, the Perturbed Matrix Method, the redox potential of the three species has been calculated and after validation by comparison with experimental results, insights were gained into the structural and dynamic determinants to the redox thermodynamics of the mutants.

The analyses here performed reveal that the experimental raise of E^0 determined by the mutations cannot be ascribed to a general mechanism but that a site-specific analysis is necessary to clarify the effect exerted by each mutation.

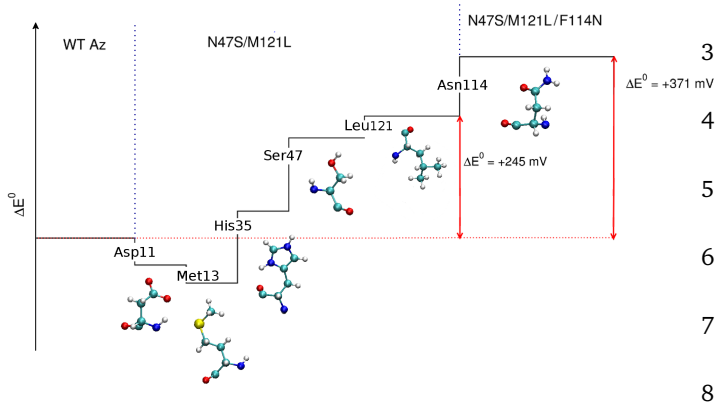

Fig. 8 Schematic representation of the effect of the residues identified as key sites in raise or lower E^0.

The changes in E^0 upon mutations stem from a combination of different effects: *i)*the chemical interaction between the mutated residue and the copper when the mutation affect the core of the active site (as in the case of the M121L mutation), *ii)* the intrinsic electrostatic properties of the mutated residue (as in the case of the F114N mutation) , *iii)* the direct electrostatic interaction (such as the different electrostatic interaction between His35 and the QC upon N47S mutation) and *iv)* the dynamic interplay between specific protein regions and the active site (as in the case of the weakening of the interaction between loops 1 and 2 induced by the N47S mutation or of the change in the HB pattern of residue 114 induced by the F114N mutation).

Most notably, the approach here applied allows for the estimation of the individual contribution of each residue to the overall electrostatic potential exerted on the protein active site, both in terms of magnitude and sign. A small number of residues are identified as key sites in raising and lowering E^0, as schematically shown in Figure 8. This enables the identification of other sites that could be mutated to further expand or fine-tune the reduction potential of azurin.

Acknowledgements

The authors thank Yi Lu for fruitful discussions and helpful comments. The authors acknowledge the CINECA award IsC20_PROSURF under the ISCRA initiative for the availability of high-performance computing resources and support. LZP and SC acknowledge funding from MIUR through PRIN 2012A7LMS3 003.

References

1 O. Farver and I. Pecht, *Coord. Chem. Rev.*, 2011, **255**, 757 – 773.
2 N. M. Marshall, D. K. Garner, T. D. Wilson, Y.-G. Gao, H. Robinson, M. J. Nilges and Y. Lu, *Nature*, 2009, **462**, 113–116.
3 N. Sailasuta, F. C. Anson and H. B. Gray, *J. Am. Chem. Soc.*, 1979, **101**, 455–458.
4 A. Sykes, *Active-Site Properties Of The Blue Copper Proteins*, Academic Press, 1991, vol. 36, pp. 377 – 408.
5 S. Yanagisawa, M. J. Banfield and C. Dennison, *Biochem.*, 2006, **45**, 8812–8822.
6 O. Farver, N. M. Marshall, S. Wherland, Y. Lu and I. Pecht, *Proc. Natl. Acad. Sci. USA*, 2013, **110**, 10536–10540.
7 L. Paltrinieri, M. Borsari, A. Ranieri, G. Battistuzzi, S. Corni and C. A. Bortolotti, *J. Phys. Chem. Lett.*, 2013, **4**, 710–715.
8 S. M. Berry, M. H. Baker and N. J. Reardon, *J. Inorg. Biochem.*, 2010, **104**, 1071 – 1078.
9 E. I. Solomon and R. G. Hadt, *Coord. Chem. Rev.*, 2011, **255**, 774 – 789.
10 M. V. Botuyan, A. Toy-Palmer, J. Chung, R. C. Blake II, P. Beroza, D. A. Case and H. J. Dyson, *Journal of molecular biology*, 1996, **263**, 752–767.
11 D. W. Low and M. G. Hill, *J. Am. Chem. Soc.*, 1998, **120**, 11536–11537.
12 M. C. Machczynski, H. B. Gray and J. H. Richards, *J. Inorg. Biochem.*, 2002, **88**, 375 – 380.
13 M. H. M. Olsson, G. Hong and A. Warshel, *J. Am. Chem. Soc.*, 2003, **125**, 5025–5039.
14 E. I. Solomon, R. K. Szilagyi, S. DeBeer-George and L. Basumallick, *Chem. Rev.*, 2004, **104**, 419–458.
15 H. Li, S. P. Webb, J. Ivanic and J. H. Jensen, *J. Am. Chem. Soc.*, 2004, **126**, 8010–8019.
16 D. Si and H. Li, *J. Phys. Chem. A*, 2009, **113**, 12979–12987.
17 G. Hong, D. M. Ivnitski, G. R. Johnson, P. Atanassov and R. Pachter, *J. Am. Chem. Soc.*, 2011, **133**, 4802–4809.

18 R. G. Hadt, N. Sun, N. M. Marshall, K. O. Hodgson, B. Hedman, Y. Lu and E. I. Solomon, *J. Am. Chem. Soc.*, 2012, **134**, 16701–16716.

19 L. J. C. Jeuken, P. van Vliet, M. P. Verbeet, R. Camba, J. P. McEvoy, F. A. Armstrong and G. W. Canters, *J. Am. Chem. Soc.*, 2000, **122**, 12186–12194.

20 B. Crane, A. Di Bilio, J. Winkler and H. Gray, *J. Am. Chem. Soc.*, 2001, **123**, 11623–11631.

21 L. Jeuken, L. Wisson and F. Armstrong, *Inorg. Chim. Acta*, 2002, **331**, 216–223.

22 H. B. Gray and J. R. Winkler, *Quart. Rev. Biophys.*, 2003, **36**, 341–372.

23 A. Alessandrini, M. Gerunda, G. Canters, M. P. Verbeet and P. Facci, *Chem. Phys. Lett.*, 2003, **376**, 625–630.

24 S. Corni, *J. Phys. Chem. B*, 2005, **109**, 3423–3430.

25 M. van den Bosch, M. Swart, J. G. Snijders, H. J. C. Berendsen, A. E. Mark, C. Oostenbrink, W. F. van Gunsteren and G. W. Canters, *ChemBioChem*, 2005, **6**, 738–746.

26 C. Li, S. Yanagisawa, B. M. Martins, A. Messerschmidt, M. J. Banfield and C. Dennison, *Proc. Natl. Acad. Sci. USA*, 2006, **103**, 7258–7263.

27 M. Cascella, A. Magistrato, I. Tavernelli, P. Carloni and U. Rothlisberger, *Proc. Natl. Acad. Sci. USA*, 2006, **103**, 19641–19646.

28 D. K. Garner, M. D. Vaughan, H. J. Hwang, M. G. Savelieff, S. M. Berry, J. F. Honek and Y. Lu, *Journal of the American Chemical Society*, 2006, **128**, 15608–15617.

29 K. M. Lancaster, S. D. George, K. Yokoyama, J. H. Richards and H. B. Gray, *Nature Chem.*, 2009, **1**, 711–715.

30 I. Ron, L. Sepunaru, S. Itzhakov, T. Belenkova, N. Friedman, I. Pecht, M. Sheves and D. Cahen, *J. Am. Chem. Soc.*, 2010, **132**, 4131–4140.

31 D. E. Khoshtariya, T. D. Dolidze, M. Shushanyan, K. L. Davis, D. H. Waldeck and R. van Eldik, *Proc. Natl. Acad. Sci. USA*, 2010, **107**, 2757–2762.

32 S. Monari, G. Battistuzzi, C. A. Bortolotti, S. Yanagisawa, K. Sato, C. Li, I. Salard, D. Kostrz, M. Borsari, A. Ranieri *et al.*, *J. Am. Chem. Soc.*, 2012, **134**, 11848–11851.

33 W. Li, L. Sepunaru, N. Amdursky, S. R. Cohen, I. Pecht, M. Sheves and D. Cahen, *ACS Nano*, 2012, **6**, 10816–10824.

34 M. Aschi, R. Spezia, A. Di Nola and A. Amadei, *Chem. Phys. Lett.*, 2001, **344**, 374–380.

35 R. Spezia, M. Aschi, A. Di Nola and A. Amadei, *Chem. Phys. Lett.*, 2002, **365**, 450–456.

36 A. Amadei, M. D'Abramo, C. Zazza and M. Aschi, *Chem. Phys. Lett.*, 2003, **381**, 187–193.

37 A. Amadei, F. Marinelli, M. D'Abramo, M. D'Alessandro, M. Anselmi, A. Di Nola and M. Aschi, *J. Chem. Phys.*, 2005, **122**, 124506.

38 A. Amadei, M. D'Alessandro, M. D'Abramo and M. Aschi, *J. Chem. Phys.*, 2009, **130**, 08410–08415.

39 C. A. Bortolotti, A. Amadei, M. Aschi, M. Borsari, S. Corni, M. Sola and I. Daidone, *J. Am. Chem. Soc.*, 2012, **134**, 13670–13678.

40 L. Zanetti-Polzi, I. Daidone, C. A. Bortolotti and S. Corni, *J. Am. Chem. Soc.*, 2014, **136**, 12929–12937.

41 I. Daidone, L. Paltrinieri, A. Amadei, G. Battistuzzi, M. Sola, M. Borsari and C. A. Bortolotti, *J. Phys. Chem. B*, 2014, **118**, 7554–7560.

42 J. Gao and D. G. Truhlar, *Ann. Rev. Phys. Chem.*, 2002, **53**, 467–505.

43 T. Vreven and K. Morokuma, *Ann. Rep. Comp. Chem.*, 2006, **2**, 35–51.

44 H. M. Senn and W. Thiel, *Curr. Opin. Struct. Biol.*, 2007, **17**, 182–187.

45 L. Zanetti-Polzi, A. Amadei, M. Aschi and I. Daidone, *J. Am. Chem. Soc.*, 2011, **133(30)**, 11414–11417.

46 A. Amadei, I. Daidone and M. Aschi, *Phys. Chem. Chem. Phys.*, 2012, **14**, 1360–13770.

47 A. Amadei, M. D'Alessandro and M. Aschi, *J. Phys. Chem. B*, 2004, **108**, 16250–16254.

48 I. Muegge, P. Qi, A. Wand, Z. Chu and A. Warshel, *J. Phys. Chem. B*, 1997, **101**, 825–836.

49 J. Wang, P. Cieplak and P. A. Kollman, *J. Comp. Chem.*, 2000, **21**, 1049–1074.

50 P. Comba and R. Remenyi, *J. Comp. Chem.*, 2002, **23**, 697–705.

51 W. L. Jorgensen, J. Chandrasekhar, J. D. Madura, R. W. Impey and M. L. Klein, *J. Chem. Phys.*, 1983, **79**, 926–935.

52 D. Brown and J. H. R. Clarke, *Mol. Phys.*, 1984, **51**, 1243–1252.

53 T. Darden, D. York and L. Pedersen, *J. Chem. Phys.*, 1993, **98**, 10089–10092.

54 B. Hess, H. Bekker, H. J. C. Berendsen and J. G. E. M. Fraaije, *J. Comp. Chem.*, 1997, **18**, 1463–1472.

55 H. J. C. Berendsen, D. van der Spoel and R. van Drunen, *Comp. Phys. Comm.*, 1995, **91**, 43–56.

56 G. te Velde, F. M. Bickelhaupt, E. J. Baerends, C. Fonseca Guerra, S. J. A. van Gisbergen, J. G. Snijders and T. Ziegler, *J. Comp. Chem.*, 2001, **22**, 931–967.

57 M. Swart, P. T. van Duijnen and J. G. Snijders, *J. Comp. Chem.*, 2001, **22**, 79–88.

58 T. Vreven, K. Morokuma, O. Farkas, H. B. Schlegel and M. J. Frisch, *J. Comp. Chem.*, 2003, **24**, 760–769.

59 A. K. Rappe, C. J. Casewit, K. S. Colwell, W. A. Goddard and W. M. Skiff, *J. Am. Chem. Soc.*, 1992, **114**, 10024–10035.

60 S. Grimme, *Journal of computational chemistry*, 2006, **27**,

1787–1799.

61 Y. Zhao and D. G. Truhlar, *Theor. Chem. Acc.*, 2008, **120**, 215–241.

62 A. Schafer, C. Huber and R. Ahlrichs, *J. Chem. Phys.*, 1994, **100**, 5829–5835.

63 T. Yanai, D. P. Tew and N. C. Handy, *Chem. Phys. Lett.*, 2004, **393**, 51–57.

64 M. Frisch, G. Trucks, H. Schlegel, G. Scuseria, M. Robb and J. R. Cheeseman, *Gaussian 03, Revision C.02*, Gaussian Inc., Wallingford,CT, 2004.

65 W. R. Fawcett, *Langmuir*, 2008, **24**, 9868–9875.

66 A. A. Isse and A. Gennaro, *J. Phys. Chem. B*, 2010, **114**, 7894–7899.